lajss.org
Latin American Journal of Solids and Structures
www.lajss.org

Stiffness Redistribution and Hole-Edge Stress Concentration in Thin-Walled Aluminum Shells Under Impact Loading

Xichen Deng[a], Yanqing Guo[a*], Lu Liu[a], Yanmei Wang[a], Jinhua Liu[a]

a School of Mechanical Engineering, North University of China, Taiyuan 030051, China

* Corresponding author. Email: guoyanqing@nuc.edu.cn

Abstract

Thin-walled aluminum shells with mounting holes are widely used in lightweight protective enclosures, but it remains unclear whether local stiffening or uniform thickening provides a safer balance between global deformation control and hole-edge stress margin under impact loading. This study compares a 4/4 mm baseline shell, a 4/4 mm locally stiffened shell, and a 5/5 mm uniformly thickened 6061-T6 shell under the same 300 g, 2 ms base acceleration using transient finite element analyses with identical geometry, material data, supports, loading, mesh, and solver settings. Within this linear-elastic relative-comparison framework, the locally stiffened shell reduces maximum deformation by 16.06%, yet increases the selected hole-edge peak stress by 27.76% and the unaveraged nodal peak equivalent stress by 32.52%, lowering the minimum stress-margin indicator to 0.60216. In contrast, uniform thickening reduces deformation by 42.36%, decreases the selected hole-edge stress by 5.25% and the nodal peak stress by 17.34%, and raises the indicator to 0.96538. Boundary-condition sensitivity confirms that support idealization does not reverse this trend. A supplementary elastoplastic analysis using a bilinear isotropic hardening model shows that plasticity reduces the peak nodal stress of the critical stiffened shell by 19.4%, confines yielding to a sub-millimeter hole-edge band, and preserves the linear-elastic ranking for comparative design assessment. Therefore, displacement reduction alone is insufficient for evaluating impact-loaded perforated shells. For engineering design under the specified impact condition, uniform thickening should be prioritized when balanced deformation control and local stress-margin improvement are required, while local stiffening should be paired with hole-edge reinforcement and elastoplastic assessment.

Keywords

thin-walled aluminum shell; transient impact; local stiffening; uniform thickening; stiffness redistribution; hole-edge stress concentration

Graphical Abstract

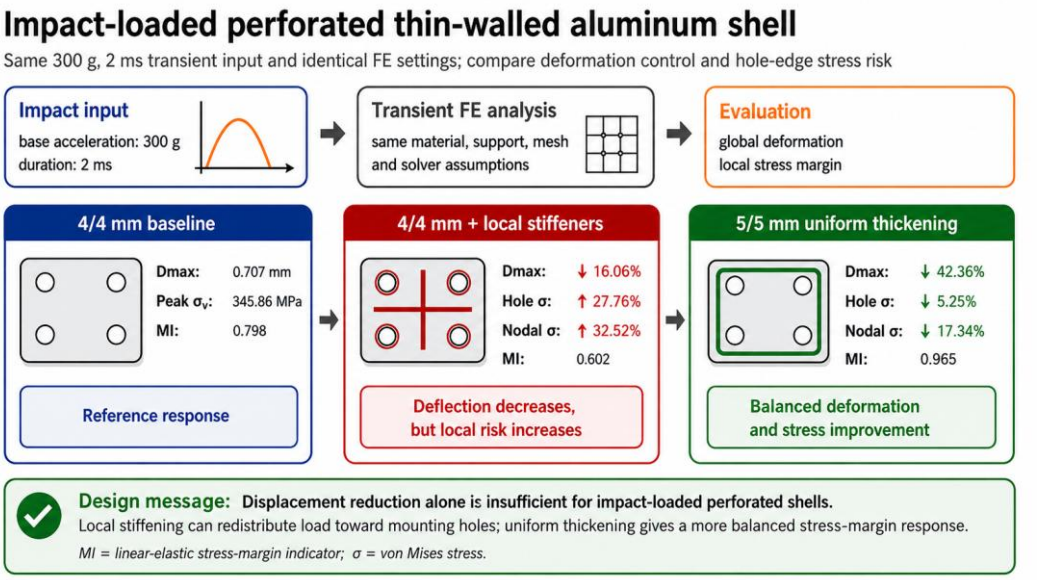

1 INTRODUCTION

Enclosed thin-walled housings are extensively used in aerospace electronics compartments, protective enclosures, and lightweight structural packaging systems, including sealed-cabin and lightweight enclosure applications (Cheng et al., 2023). Under high-overload and short-duration impact environments, these structures may experience rapid amplification of global plate deflection together with local stress concentration at mounting holes, fillet transition zones, and constrained boundaries (Yu et al., 2021; Abu-Farsakh et al., 2015). Therefore, impact-resistant assessment requires simultaneous consideration of global deformation and local stress response rather than relying on a single displacement or stress value.

Previous studies on structural impact dynamics and impulsively loaded thin plates have shown that dynamic response and failure are strongly affected by loading history, boundary conditions, material properties, and structural geometry (Yu et al., 2021; Nurick and Martin, 1989a; Nurick and Martin, 1989b). For box-type and thin-walled structures under internal, confined, underwater, or air-blast loading, numerical and experimental studies further indicate that load confinement, material strength, wall thickness, and geometric scale can govern deformation and damage response (Zhang et al., 2019; Yao et al., 2024; Nagesh and Gupta, 2021; Geretto et al., 2015; Yao et al., 2016). For stiffened plates, stiffener layout, relative stiffness, natural frequency, and power-flow paths may alter load transfer and nonlinear dynamic response (Zhao et al., 2020; Zheng et al., 2016; Li et al., 2021; Goel et al., 2011; Jiang et al., 2023; Yuen and Nurick, 2005; Langdon et al., 2005; Cao et al., 2019; Xu et al., 2005). In addition, studies on plates with openings indicate that holes can significantly change dynamic response and local stress concentration (Li et al., 2017; Abu-Farsakh et al., 2015).

Despite these advances, the relative merits of uniform thickening and local stiffening remain insufficiently clarified for closed thin-walled shells with mounting holes when the same material parameters, boundary conditions, impact input, and evaluation criteria are maintained. In particular, a stiffener may suppress global plate deflection while redirecting load transfer toward holes or stiffness-transition regions. This creates a practical design question: whether a locally stiffened shell is always safer than a uniformly thickened shell when both deformation control and local stress margin are considered.

To address this question, this study compares a 4/4 mm baseline shell, a 4/4 mm locally stiffened shell, and a 5/5 mm uniformly thickened shell under identical transient impact loading. The objective is not only to compare three geometries, but also to clarify how stiffness redistribution, while suppressing global deformation, can simultaneously intensify hole-edge stress concentration in a closed perforated thin-walled shell. Similar comparative numerical strategies have been used for box-type, stiffened, and lightweight enclosure structures under transient loading, where deformation and local damage indicators are evaluated together (Zhang et al., 2019; Li et al., 2021; Yao et al., 2024; Yao et al., 2016; Cheng et al., 2023).

The main contribution of this study is the identification of a stiffness-redistribution mechanism through which local stiffening can reduce global deflection while increasing local stress concentration around mounting holes and transition regions. Unlike studies that focus mainly on maximum deformation reduction, this work jointly evaluates global deformation, unaveraged nodal peak equivalent stress, a linear-elastic stress-margin indicator, and mass-related efficiency. This multi-indicator perspective complements previous studies on plate deformation, blast response, and stiffener layout effects (Zhao et al., 2020; Goel et al., 2011; Yuen and Nurick, 2005; Langdon et al., 2005; Cao et al., 2019).

Specifically, this study: (i) conducts a comparative finite element assessment of uniform thickening and local stiffening under the same transient impact input, material parameters, and boundary conditions; (ii) demonstrates that local stiffening may reduce global deformation while aggravating stress concentration near mounting holes; (iii) interprets the result from the viewpoint of stiffness redistribution and load-transfer-path concentration; (iv) introduces a mass-related efficiency comparison to judge whether deformation, stress, and stress-margin improvements are sufficient to compensate for the mass increase; and (v) examines the robustness of the main trend through a boundary-condition sensitivity check on the hole-support idealization.

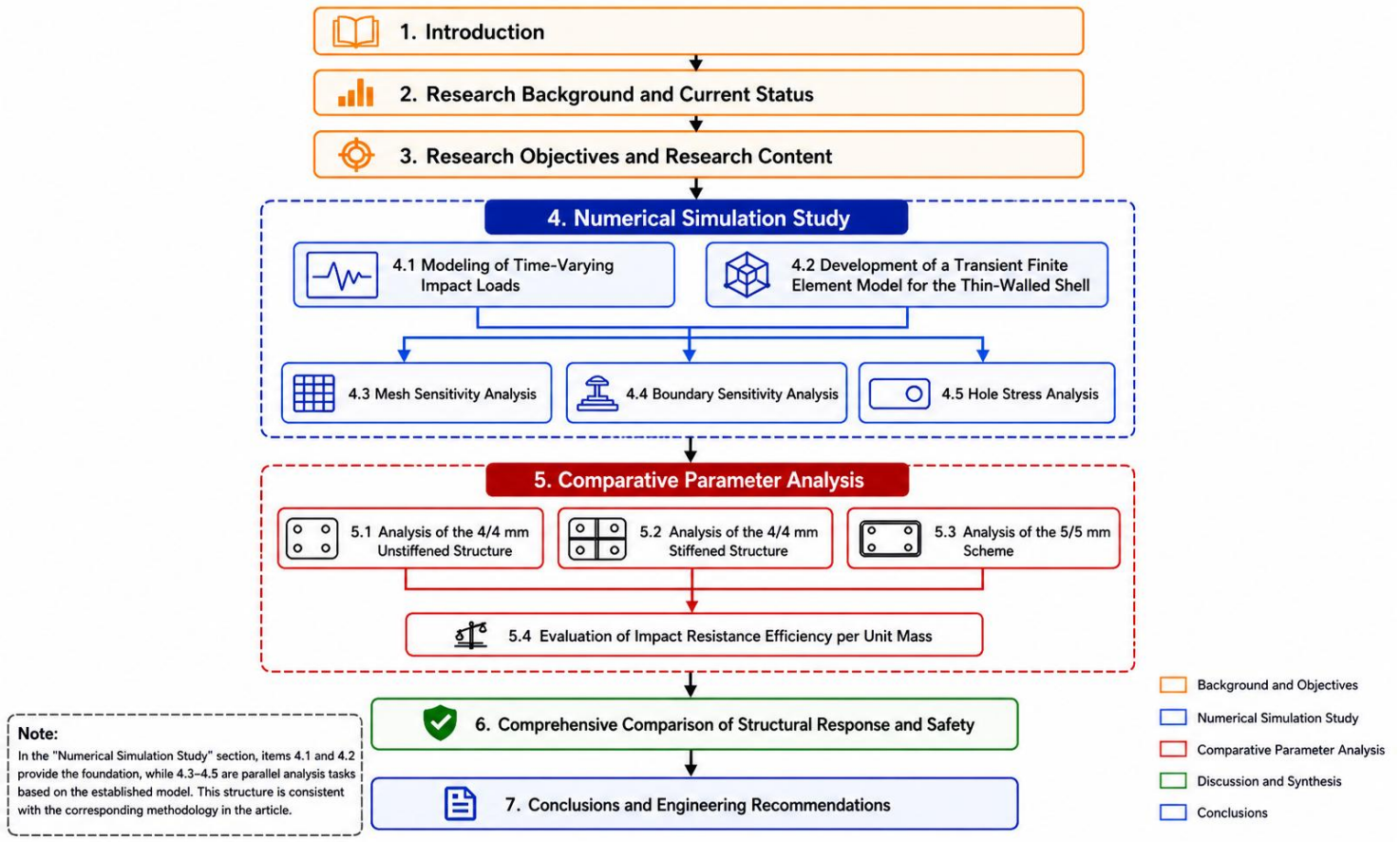

Figure 1. Research roadmap of the numerical assessment.

2 MODEL AND LOADING CONDITIONS

2.1 Geometric model, material properties and boundary conditions

The study focuses on a rectangular closed thin-walled shell with external dimensions of approximately 300 mm × 200 mm × 100 mm. The material is 6061-T6 aluminum alloy, with a density of 2700 kg/m³, an elastic modulus of 69 GPa, a Poisson ratio of 0.33, a yield strength of 276 MPa, and a tensile strength of 310 MPa. To ensure comparability, the three models maintain the same external dimensions, material properties, mounting-hole arrangement, loading history, and constraint strategy. The only variables are the wall-thickness configuration and the introduction of local stiffeners. The selection of a closed shell with mounting holes is consistent with lightweight enclosure and perforated-plate applications in which geometric discontinuities often govern local stress concentration (Li et al., 2017; Abu-Farsakh et al., 2015; Cheng et al., 2023).

The notation 4/4 mm means that both the sidewall and base-plate thicknesses are 4 mm, whereas 5/5 mm means that both thicknesses are 5 mm. The notation 4/4 mm + stiffeners denotes the 4/4 mm baseline shell with cross-shaped local stiffeners added to the inner large-plate surfaces. For all schemes, the inner surfaces of the mounting holes are constrained to approximate a rigid bolted-support condition. This idealized constraint is adopted to maintain a controlled comparison among the schemes, but it may conservatively amplify local hole-edge stresses. The geometric models of the three shell configurations are illustrated in Figure 2.

For reproducibility, the main geometric parameters extracted from the CAD/STEP models are summarized in Table 1. The coordinates are reported in the exported STEP coordinate system, where the shell envelope is defined by x = −150 to 150 mm, y = −50 to 50 mm, and z = −200 to 0 mm.

Table 1. Detailed geometric parameters of the three structural schemes.

Parameter	Value / definition	Applicable scheme(s)
External dimensions	300 mm × 200 mm × 100 mm; STEP envelope x = −150 to 150 mm, z = −200 to 0 mm, y = −50 to 50 mm	All schemes

Wall/base-plate thickness	4/4 mm for the baseline and locally stiffened shells; 5/5 mm for the uniformly thickened shell	All schemes
Mounting-hole diameter	5 mm (radius 2.5 mm)	All schemes
Mounting-hole axis and through-thickness range	Hole axis along the y-direction. The through-thickness range is y = −50 to −46 mm for the 4/4 mm shells and y = −50 to −45 mm for the 5/5 mm shell.	All schemes
Hole-center coordinates in the x–z plane	(−130, −20), (130, −20), (−130, −180), and (130, −180) mm	All schemes
Center-to-edge distance	20 mm from each hole center to the nearest outer x-edge and z-edge	All schemes
Hole-edge clearance	17.5 mm from the hole edge to the nearest outer x-edge and z-edge	All schemes
Hole-center spacing	260 mm in the x-direction and 160 mm in the z-direction	All schemes
Corner / transition radii	Outer shell corner radius R = 5 mm; inner offset/transition radius R = 4 mm. No additional stiffener-end or stiffener-root fillet is modeled.	All schemes; last sentence applies to the stiffened scheme
Stiffener width and height	Rectangular rib width = 2 mm; rib height = 8 mm measured from the inner plate surface.	4/4 mm + stiffeners
Stiffener longitudinal rib (z-direction rib)	x ≈ −0.989 to 1.011 mm (2 mm width); z ≈ −188.000 to −12.000 mm (effective length ≈ 176 mm)	4/4 mm + stiffeners
Stiffener transverse rib (x-direction rib)	z = −101 to −99 mm (2 mm width); x ≈ −137.989 to 138.011 mm (effective length ≈ 276 mm)	4/4 mm + stiffeners
Stiffener placement	The cross-shaped ribs are arranged on the inner large-plate surfaces, occupying y = −46 to −38 mm and y = 38 to 46 mm in the STEP model.	4/4 mm + stiffeners

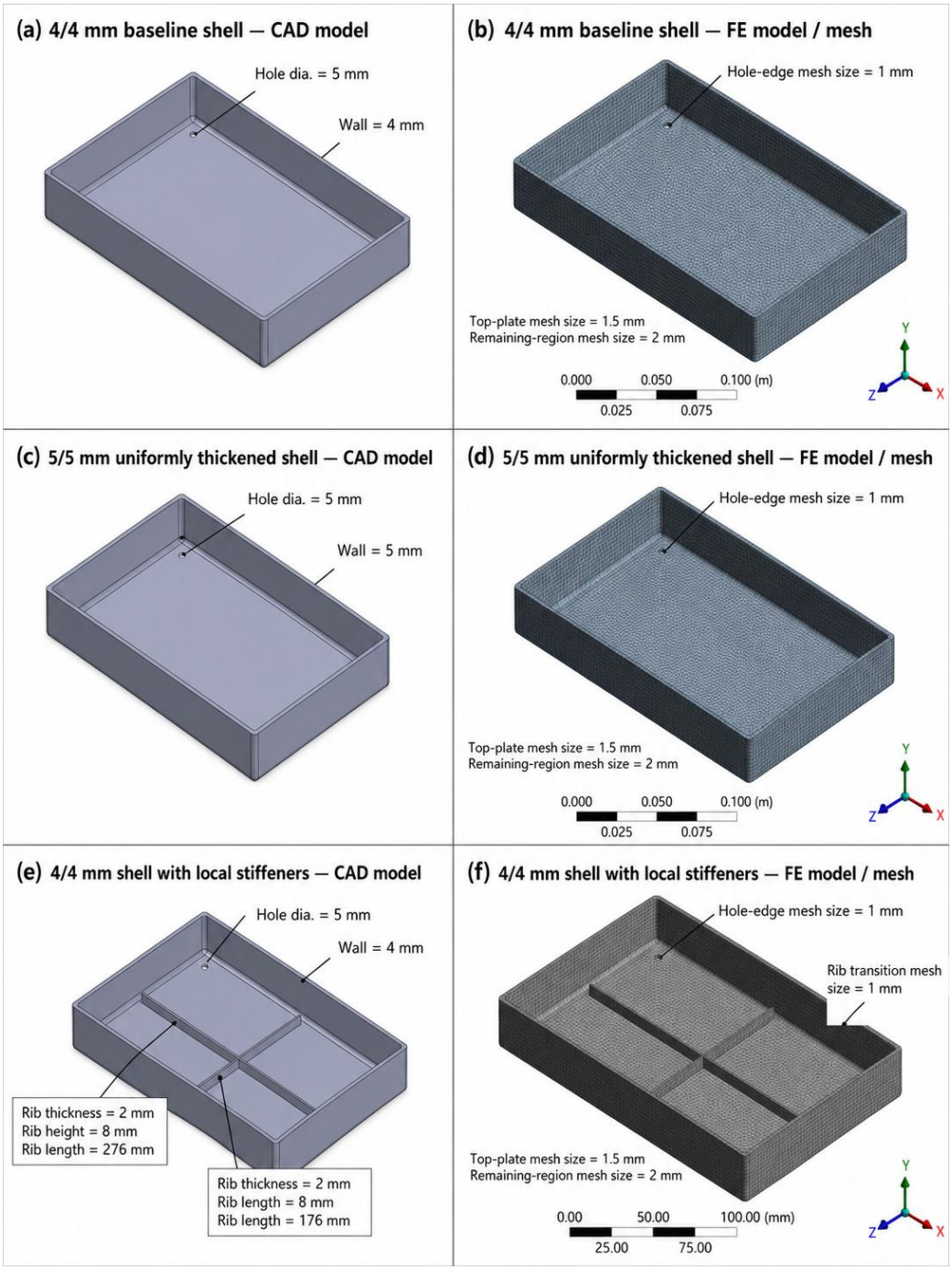

Figure 2. Geometric and finite element models of the three shell configurations.

The hole coordinates and clearances are identical among the three schemes so that the effects of wall-thickness change and local stiffening can be compared without changing the mounting-hole arrangement. For the stiffener coordinate ranges in Table 1, the narrow x- or z-interval denotes the rib width, whereas the effective length is measured along the rib axis.

This boundary condition should be interpreted as a conservative constraint case rather than a full bolted-joint simulation, since boundary flexibility, bolt preload, contact friction, and possible joint clearance are not explicitly modeled. The results are therefore used mainly to compare relative structural response as well as to identify critical stress regions under a consistent modeling framework.

Time-history impact inputs are commonly adopted in structural impact dynamics to represent short-duration dynamic loading and to compare transient structural responses under controlled loading histories (Yu et al., 2021; Nurick and Martin, 1989a; Nurick and Martin, 1989b). Therefore, the Y-direction base acceleration used to characterize the

shock input is defined by a piecewise linear function based on selected time-acceleration points (t_i, a_i). When a given time t falls between two adjacent sampling points, the acceleration can be expressed as:

$$a(t) = a_i + [(a_{i+1} - a_i)/(t_{i+1} - t_i)](t - t_i), \quad t_i \le t \le t_{i+1} \tag{1}$$

The inertial effect of the structure in the direction of impact can be equated to:

$$F(t) = m\, a(t) \tag{2}$$

where a(t) represents the time-varying impact acceleration in mm/s², F(t) denotes the equivalent inertial load, and m denotes the structural mass. According to Table 2, the peak acceleration is approximately 2.943×10^6 mm/s², corresponding to about 300 g. Such acceleration-based loading is particularly suitable for preliminary comparison of lightweight shell responses when the objective is relative structural assessment rather than full impact-contact reconstruction (Yu et al., 2021; Zhang et al., 2019; Yao et al., 2016).

The discrete time-acceleration input points used for the piecewise linear interpolation are listed in Table 2. The last zero-acceleration point at 6 ms is retained to define the post-pulse zero level, while the comparative transient analyses use the response within the main impact window.

Table 2. Time-acceleration input points for the Y-direction base acceleration.

Point	Time / s	Time / ms	Acceleration / mm·s^{-2}	Acceleration / g
1	0	0	0	0.00
2	2.0e-4	0.2	9.94e+5	101.33
3	4.0e-4	0.4	1.73e+6	176.35
4	6.0e-4	0.6	2.381e+6	242.71
5	8.0e-4	0.8	2.799e+6	285.32
6	1.0e-3	1	2.943e+6	300.00
7	1.2e-3	1.2	2.799e+6	285.32
8	1.4e-3	1.4	2.381e+6	242.71
9	1.6e-3	1.6	1.73e+6	176.35
10	1.8e-3	1.8	9.094e+5	92.70
11	2.0e-3	2	0	0.00
12	6.0e-3	6	0	0.00

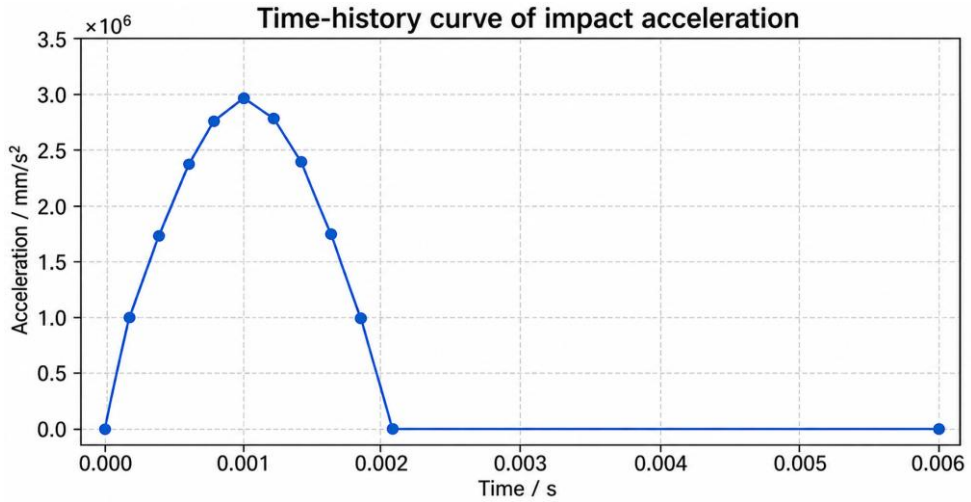

Figure 3. Time-history curve of shock acceleration.

2.2 Numerical solutions and evaluation indicators

The ANSYS transient structural analysis module is used to obtain the dynamic response through full transient analysis with Hilber-Hughes-Taylor (HHT) time integration. The finite element model uses three-dimensional SOLID187

elements. Unless otherwise stated, the same material parameters, boundary conditions, acceleration history, element type, mesh strategy, and time-step settings are maintained for all structural schemes to ensure comparability. According to the ANSYS solver-output terminology, the HHT transient parameters are $\gamma = 0.1000$, $\alpha = 0.3025$, $\delta = 0.6000$, $\alpha_f = 0.1000$, and $\alpha_m = 0.0000$. Automatic time stepping is used with an initial time step of 5.0×10^{-6} s, a minimum time step of 1.0×10^{-6} s, a maximum time step of 2.0×10^{-5} s, and a load-step end time of 3.0×10^{-3} s.

The selected HHT parameters are used to introduce high-frequency numerical damping and to suppress spurious oscillations that can occur during short-duration impact simulations. The same integration parameters are applied to all structural schemes, hence they do not affect the relative comparison among the baseline, locally stiffened, and uniformly thickened models.

The evaluation indices are selected at four levels: global deformation, local stress concentration, local linear-elastic stress margin, and mass-related design efficiency. The maximum total deformation characterizes overall stiffness and deflection-control capability. The unaveraged nodal peak equivalent stress is used as a conservative local stress-concentration indicator, while the minimum linear-elastic stress-margin indicator describes the relative elastic margin in hazardous regions. Full transient finite element analysis has been widely used for box walls, stiffened plates, and thin-walled plates subjected to blast or impact-type loading, especially when deformation and stress evolution are evaluated simultaneously (Zhang et al., 2019; Zhao et al., 2020; Li et al., 2021; Yao et al., 2024; Yao et al., 2016).

$$n = \sigma_s / \sigma_v \tag{3}$$

where σ_s represents the yield strength of the 6061-T6 aluminum alloy and σ_v denotes the peak von Mises equivalent stress at the critical node. Because the vicinity of the mounting holes and boundary transition zones is sensitive to local extremes, unaveraged nodal stresses are used to highlight potential hazardous zones. This value is not interpreted as a mesh-independent failure stress or as a post-yield stress prediction when local yielding may occur. Instead, it is used for relative comparison and risk-region identification under the same mesh strategy. The emphasis on local stress around holes is supported by prior studies showing that openings and material nonlinearity can strongly affect local stress concentration and damage-prone regions (Li et al., 2017; Abu-Farsakh et al., 2015).

2.3 Definition of structural schemes and main parameters

Table 3. Summary of the main indicators for the three structural schemes.

Scheme	Mass / kg	Maximum total deformation / mm	Nodal peak equivalent stress / MPa	Minimum linear-elastic stress-margin indicator
4/4 mm	2.25967	0.70721	345.86	0.79801
4/4 mm + stiffeners	2.29091	0.59362	458.35	0.60216
5/5 mm	2.79570	0.40761	285.90	0.96538

2.4 Mesh sensitivity analysis

To evaluate the influence of mesh size on the results, a mesh sensitivity analysis is conducted for the 4/4 mm baseline scheme. The mesh sizes for the coarse, medium, and fine meshes at the hole edge, top plate, and remaining regions are 1.5/2.0/2.5 mm, 1.0/1.5/2.0 mm, and 0.7/1.0/1.5 mm, respectively. The same material parameters, boundary conditions, impact load, and transient analysis settings are applied to all three mesh models, and the fine mesh model is solved using the Sparse Direct solver. Mesh refinement around openings and large-span plate regions are necessary because both thin-plate deformation and local stress concentration are sensitive to geometric discontinuities and numerical discretization (Li et al., 2017; Nurick and Martin, 1989a; Nurick and Martin, 1989b; Abu-Farsakh et al., 2015).

Table 4. Mesh sensitivity analysis results for the 4/4 mm baseline scheme.

Mesh level	Mesh size (hole/top/others, mm)	Elements	Maximum total deformation / mm	Nodal peak equivalent stress / MPa	Minimum linear-elastic stress-margin indicator
Coarse mesh	1.5 / 2.0 / 2.5	148138	0.70416	292.20	0.94454
Medium mesh	1.0 / 1.5 / 2.0	259065	0.70721	345.86	0.79801
Fine mesh	0.7 / 1.0 / 1.5	612295	0.70898	389.27	0.70901

As the mesh is refined, the maximum total deformation increases from 0.70416 mm to 0.70898 mm, with an overall variation of less than 1%. This indicates that the global bending deformation is essentially converged. In contrast, the nodal peak equivalent stress increases from 292.20 MPa to 389.27 MPa, and the minimum linear-elastic stress-margin indicator decreases from 0.94454 to 0.70901. It shows the local peak stress around the mounting holes remains mesh-sensitive. Therefore, the deformation response is used for quantitative comparison, whereas the unaveraged nodal peak stress is treated as a conservative hazardous-zone indicator and a relative comparison metric rather than a mesh-independent failure prediction. Considering computational cost and comparison consistency, the medium mesh is adopted for the comparative analyses. This treatment is consistent with impact-response studies, in which global deformation is usually more stable than highly localized peak stress under mesh refinement (Zhang et al., 2019; Zhao et al., 2020; Yao et al., 2024; Nurick and Martin, 1989a).

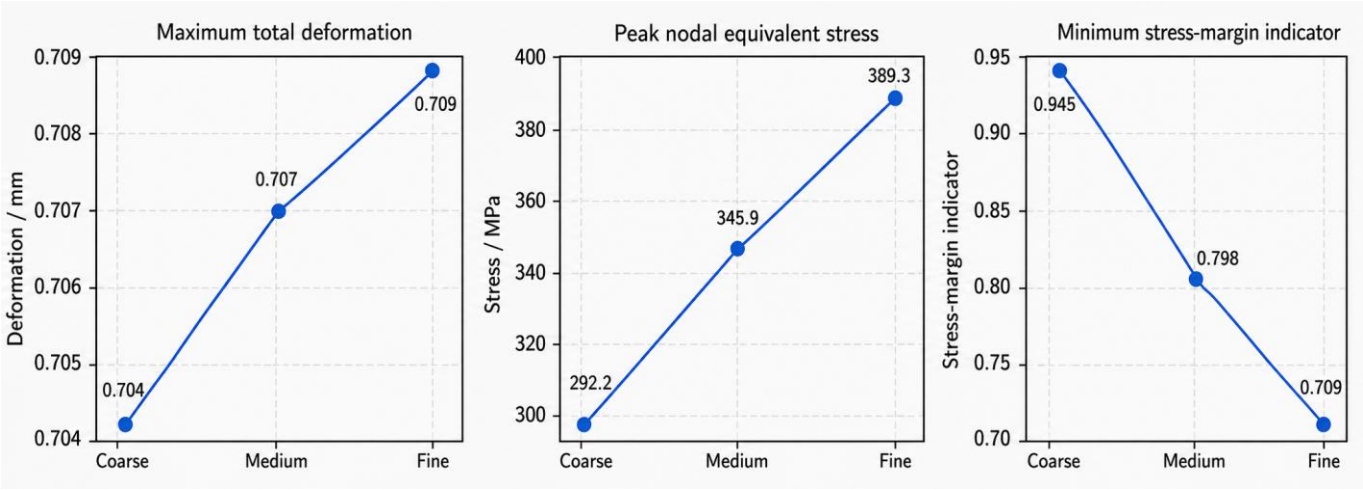

Figure 4. Mesh sensitivity curves for the 4/4 mm baseline scheme.

2.5 Boundary-condition sensitivity check

Because the main comparative model constrains the inner surfaces of the mounting holes, a boundary-condition sensitivity check is conducted to examine whether the main conclusion depends on the fixed-hole idealization. In the sensitivity model, the fixed-hole support is replaced by a relaxed hole-support condition corresponding to a modified cylindrical/frictionless constraint. The radial and axial translations of the hole surfaces are constrained, while the tangential motion is released for three holes; one reference hole is kept fully constrained to suppress rigid-body motion. Although it is still not a complete contact-preload bolt model, this setting represents a less restrictive bolted-support idealization than fully fixed hole surfaces.

All other settings are kept unchanged, including geometry, material parameters, mesh strategy, acceleration history, element type, and transient solution. For the 4/4 mm + stiffeners sensitivity model, the solver output confirms a model scale of 1,263,721 nodes and 798,818 SOLID187 elements, full transient HHT integration, automatic time stepping, a final analysis time of 3.0×10^{-3} s, and zero error messages. Therefore, the sensitivity check is used to assess the robustness of the relative trends rather than to reproduce detailed bolt-contact mechanics.

Table 5. Boundary-condition sensitivity results for the baseline and locally stiffened schemes.

Boundary condition	Scheme	Maximum total deformation / mm	Nodal peak equivalent stress / MPa	Minimum linear-elastic stress-margin indicator
Fixed hole support	4/4 mm	0.70721	345.86	0.79801
Relaxed hole support	4/4 mm	0.70853	357.42	0.77220
Fixed hole support	4/4 mm + stiffeners	0.59362	458.35	0.60216
Relaxed hole support	4/4 mm + stiffeners	0.59442	434.03	0.63590

Compared with the fixed-hole baseline, the relaxed hole support changes the maximum deformation of the 4/4 mm scheme by only 0.19%, increases the peak stress by 3.34%, and decreases the stress-margin indicator by 3.23%. For the locally stiffened scheme, the deformation changes by only 0.13%, the peak stress decreases from 458.35 MPa to 434.03 MPa and the stress-margin indicator increases from 0.60216 to 0.63590, indicating that the fully fixed hole boundary gives a conservative local stress level for this scheme.

More importantly, the locally stiffened scheme still reduces the maximum deformation from 0.70853 mm to 0.59442 mm, corresponding to a 16.10% reduction, while the nodal peak equivalent stress increases from 357.42 MPa to 434.03 MPa and the stress-margin indicator decreases from 0.77220 to 0.63590 under the relaxed hole-support condition. Thus, the absolute hole-edge peak stress is affected by the support idealizations, however the main trend remains unchanged: local stiffening improves global deformation control while maintaining a stronger local stress-concentration tendency than the 4/4 mm baseline scheme.

3 SIMULATION RESULTS AND MECHANISM INTERPRETATION

3.1 4/4 mm baseline scheme

With the critical response occurring at approximately 1.18×10^{-3} s, the maximum total deformation of the 4/4 mm baseline scheme is 0.70721 mm. Clear bulging deformation appears in the central region of the plate, indicating insufficient global bending stiffness under the specified impact input. The nodal peak equivalent stress reaches 345.86 MPa, and the hazardous region is mainly concentrated around the mounting holes and boundary transition zones. The minimum linear-elastic stress-margin indicator is 0.79801. These results show a typical response characteristic of perforated thin-walled shells: the central plate region governs global deformation, whereas the mounting holes govern local stress risk. This deformation-local-risk separation is consistent with the response characteristics of impulsively loaded and perforated plates (Li et al., 2017; Nurick and Martin, 1989a; Nurick and Martin, 1989b; Abu-Farsakh et al., 2015).

3.2 4/4 mm locally stiffened scheme

Compared with the 4/4 mm baseline scheme, the maximum total deformation of the 4/4 mm locally stiffened scheme decreases to 0.59362 mm, corresponding to a reduction of approximately 16.06%. This confirms that the stiffener enhances the bending stiffness of the large-span plate region. However, under the linear-elastic assumption, the nodal peak equivalent stress increases to 458.35 MPa, and the minimum linear-elastic stress-margin indicator decreases to 0.60216. A key finding of this study is therefore that a smaller deformation contour does not necessarily imply a larger local stress margin. Previous studies on stiffened plates also show that stiffeners can improve deformation resistance while changing stress distribution and local response, depending on reinforcement layout and loading form (Zhao et al., 2020; Zheng et al., 2016; Goel et al., 2011; Yuen and Nurick, 2005; Langdon et al., 2005; Cao et al., 2019).

The locally stiffened scheme should therefore not be viewed as ineffective, but as mechanically incomplete. The current stiffener layout changes the stiffness distribution and load-transfer path, causing a larger portion of the internal force to be transmitted toward the mounting holes and boundary transition regions. These locations already contain geometric discontinuities and constraint changes, hence they are prone to stress concentration. As a result, global deflection is reduced, but the local linear-elastic stress margin is weakened. Since the peak stress of this scheme exceeds the tensile strength of 6061-T6 aluminum alloy in the linear-elastic analysis, it should not be interpreted as an acceptable standalone optimization solution without hole-edge reinforcement and elastoplastic verification. This result is mechanically consistent with previous findings on relative stiffness, power-flow paths, and hole-induced stress concentration in stiffened or perforated plate structures (Jiang et al., 2023; Li et al., 2017; Xu et al., 2005; Abu-Farsakh et al., 2015).

3.3 5/5 mm uniformly thickened scheme

The maximum total deformation of the 5/5 mm uniformly thickened scheme is 0.40761 mm, representing a reduction of 42.36% compared with the 4/4 mm baseline scheme. The nodal peak equivalent stress decreases to 285.90 MPa, and the minimum linear-elastic stress-margin indicator increases to 0.96538. Although the indicator remains slightly below unity under the current unaveraged nodal-stress criterion, the hazardous level around the mounting holes is clearly reduced compared with the 4/4 mm baseline as well as the 4/4 mm locally stiffened schemes. Compared with local stiffening, uniform thickening enhances the overall bending stiffness without introducing an abrupt local stiffness mutation. This results in a more balanced relationship among global deformation control, local stress reduction, and elastic stress margin. This behavior is consistent with studies showing that wall thickness, structural scale, and lightweight enclosure design strongly affect the dynamic response of thin-walled structures (Zhang et al., 2019; Yao et al., 2024; Yao et al., 2016; Cheng et al., 2023).

3.4 Comprehensive comparison and mechanism interpretation

The comparison of the three schemes reveals different rankings for global and local response indicators. In terms of global deflection control, the 5/5 mm uniformly thickened scheme performs best, followed by the 4/4 mm locally stiffened scheme and then the 4/4 mm baseline scheme. In terms of local stress and elastic stress margin, the 5/5 mm

scheme remains the best, while the 4/4 mm locally stiffened scheme becomes the worst. This result shows that displacement reduction alone is an unreliable criterion for impact-resistant design. It is also consistent with prior observations that deformation control and local failure risk do not necessarily improve simultaneously in stiffened or perforated thin-walled structures (Zhao et al., 2020; Goel et al., 2011; Li et al., 2017; Abu-Farsakh et al., 2015).

Mechanistically, uniform thickening reduces deformation by increasing global bending stiffness while avoiding a sharp local stiffness transition. Local stiffening mainly redistributes stiffness in space. It suppresses deformation in the plate region. However, it redirects part of the load-transfer path toward openings and boundary transition zones. The contour comparisons in Figures 6-8 support the following interpretation: the locally stiffened model shows a smaller global deflection field but a more pronounced local stress concentration and a lower stress-margin region near the constrained holes. Therefore, the assessment combines deformation, stress, a linear-elastic stress-margin indicator, and mass-related efficiency rather than relying solely on maximum deformation. The mechanism can also be interpreted using previous findings on relative stiffness, load-transfer paths, and hole-edge stress concentration in stiffened or perforated plates (Jiang et al., 2023; Li et al., 2017; Xu et al., 2005; Abu-Farsakh et al., 2015).

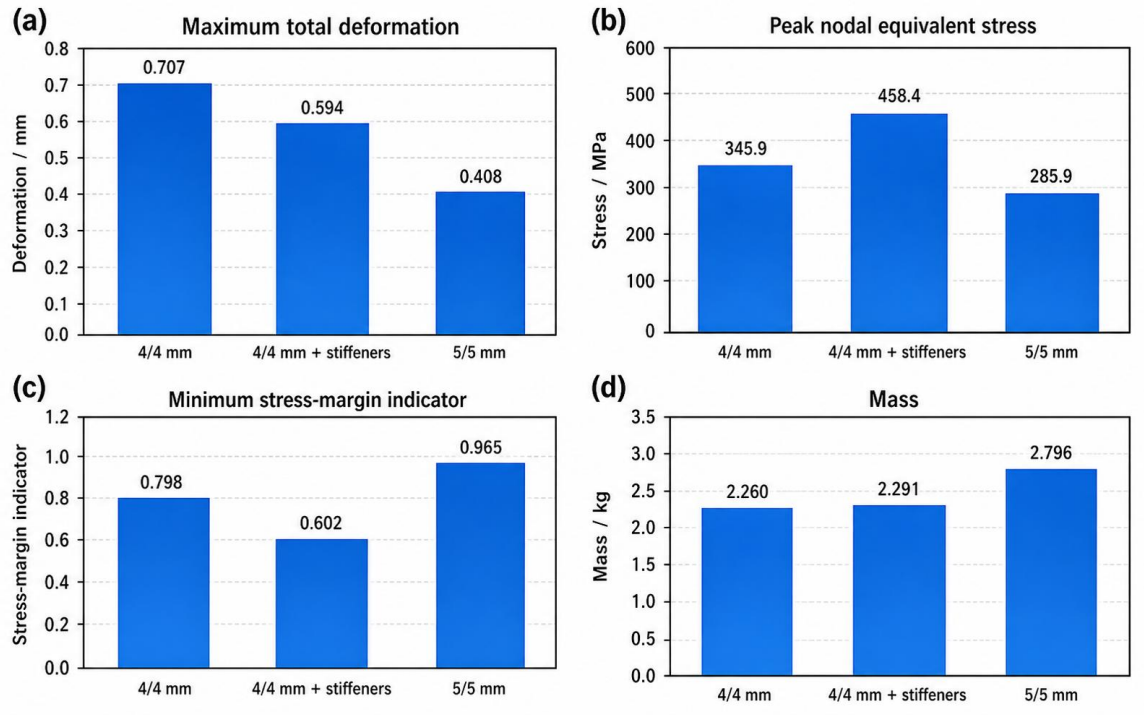

Figure 5. Comparison of the main indicators of the three schemes.

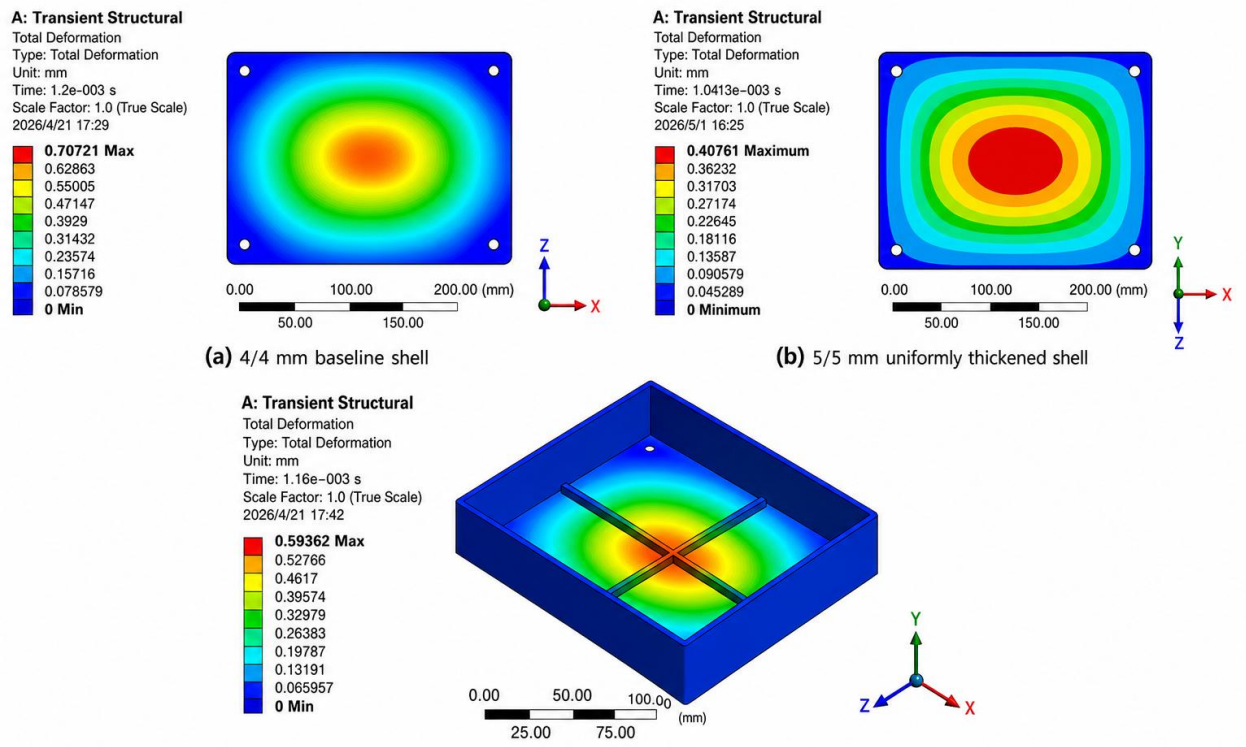

(a) 4/4 mm baseline shell

(b) 5/5 mm uniformly thickened shell

(c) 4/4 mm shell with local stiffeners

Figure 6. Comparison of total deformation contours for the three schemes.

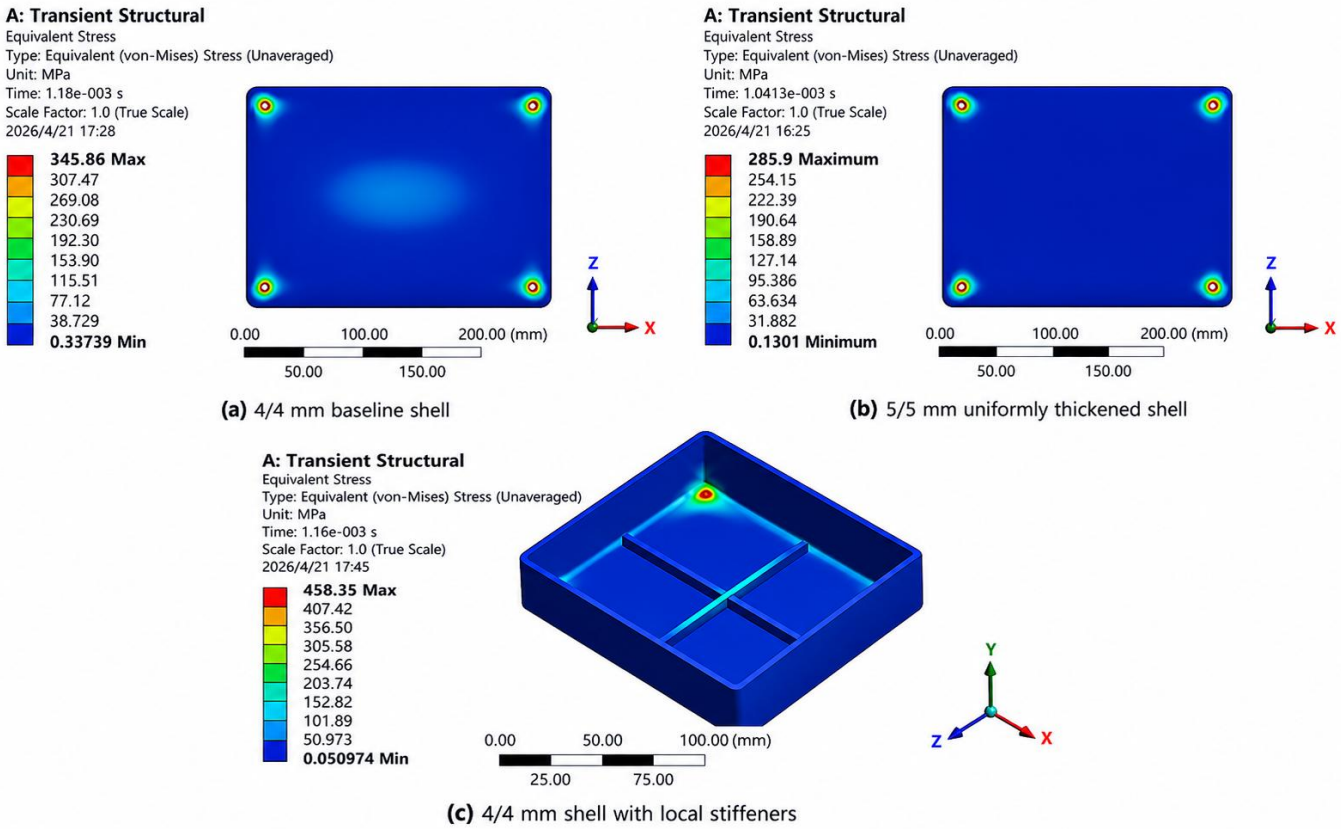

(a) 4/4 mm baseline shell

(b) 5/5 mm uniformly thickened shell

(c) 4/4 mm shell with local stiffeners

Figure 7. Comparison of unaveraged nodal equivalent-stress contours for the three schemes.

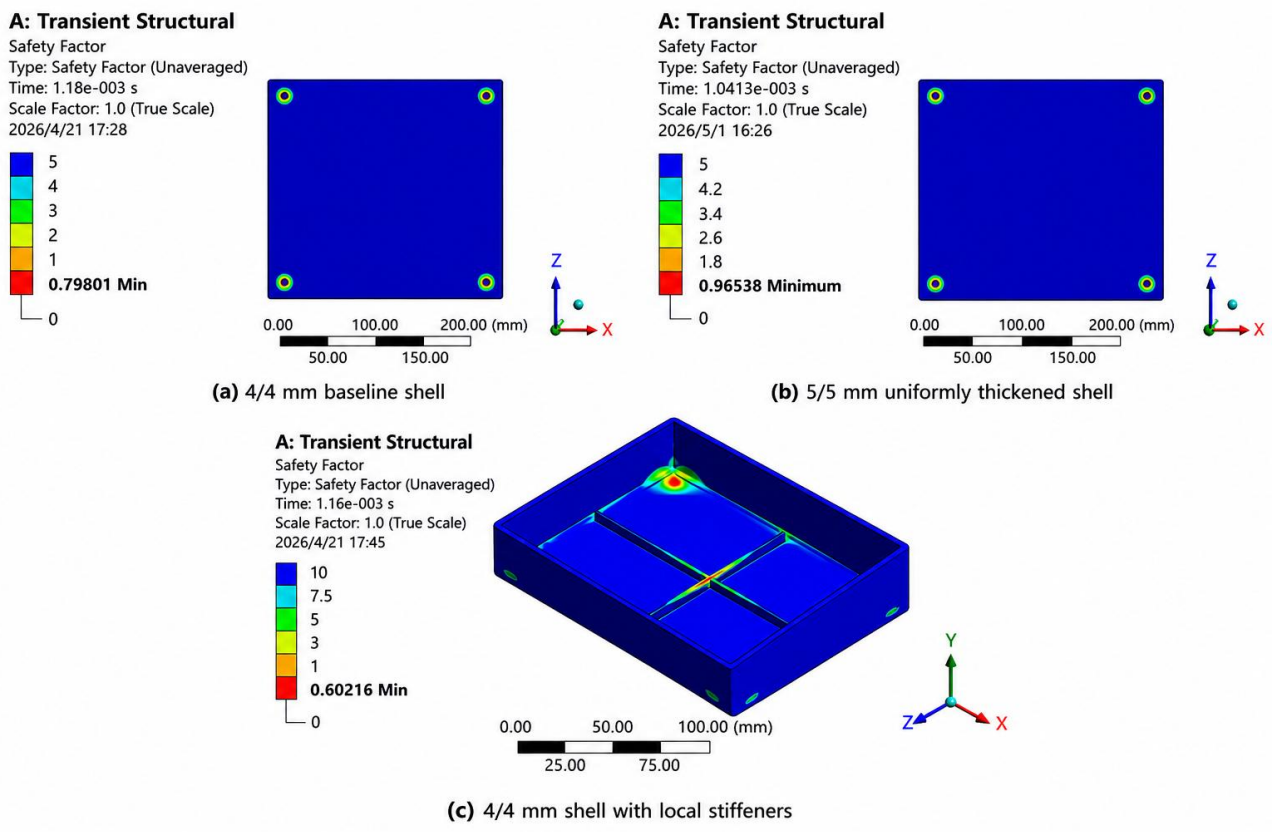

Figure 8. Comparison of linear-elastic stress-margin indicator contours for the three schemes.

To provide direct time-history evidence for the proposed stiffness-redistribution mechanism, the maximum unaveraged equivalent stress in a selected hole-edge region was extracted for all three structural schemes. To ensure the steep stress gradient nearest to the hole edge can be captured consistently in all models, the selected hole-edge region is defined as the annular band of elements surrounding each mounting hole, with a radial width of approximately one to two local element layers.

As shown in Figure 9, the 4/4 mm locally stiffened shell reaches a selected hole-edge peak of 359.79 MPa at approximately 1.16 ms, whereas the 4/4 mm baseline shell reaches 281.62 MPa at 1.18 ms and the 5/5 mm uniformly thickened shell reaches 266.84 MPa at 1.02 ms. Thus, relative to the baseline, local stiffening increases the selected hole-edge stress peak by about 27.76%, while uniform thickening decreases it by about 5.25%. This directly confirms that the current stiffener layout suppresses global deformation at the cost of intensified local hole-edge stress concentration.

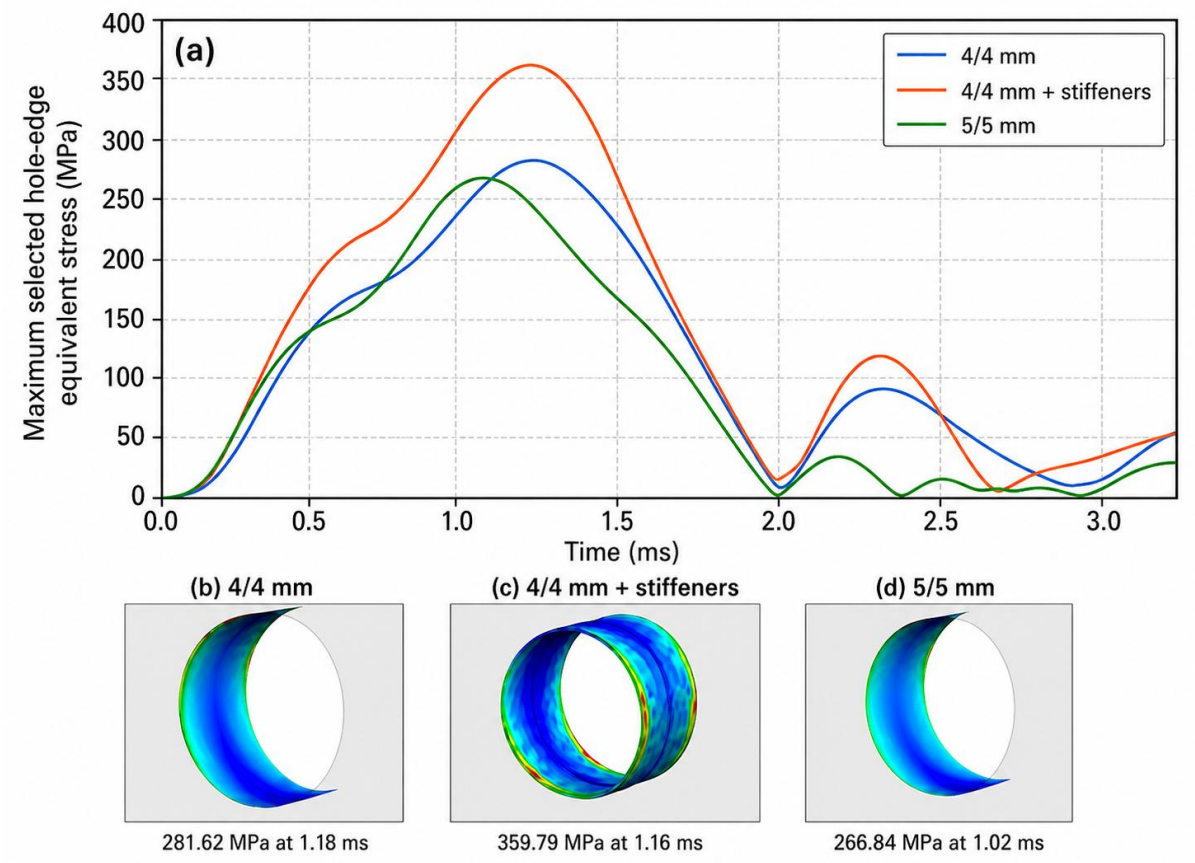

Figure 9. Time-history and local contour evidence of hole-edge stress concentration. (a) Time histories of the maximum unaveraged equivalent stress in the selected hole-edge region. (b-d) Local contours at the peak hole-edge stress time for the 4/4 mm baseline shell, 4/4 mm shell with local stiffeners, and 5/5 mm uniformly thickened shell, respectively.

3.5 Evaluation of Plastic Effect on Stress Concentration

The linear-elastic analysis presented in Sections 3.2-3.4 yields a peak unaveraged nodal von Mises stress of 458.35 MPa at the stiffener-reinforced hole edge of the 4/4 mm + stiffener shell, which substantially exceeds both the yield strength (276 MPa) and the ultimate tensile strength (310 MPa) of 6061-T6 aluminum alloy. This result is intrinsically a consequence of the linear-elastic assumption, which imposes no upper bound on stress magnitude at geometric discontinuities. To assess the extent to which material nonlinearity modifies the stress state, a supplementary elastoplastic transient analysis was conducted for the most critical configuration (4/4 mm + stiffeners).

The elastoplastic model employs a bilinear isotropic hardening (BISO) constitutive law with an initial yield stress of 276 MPa and a tangent modulus Et = 500 MPa, representing a conservative post-yield hardening slope typical of 6061-T6 aluminum (ASM Handbook, 1990). Large-deformation effects (NLGEOM) were activated, and the same acceleration pulse, mesh strategy, and boundary conditions as in the linear analysis were retained to ensure direct comparability.

Table 7. Comparison of linear-elastic and elastoplastic responses for the 4/4 mm + stiffener shell.

Indicator	Linear-elastic	Elastoplastic (BISO)	Change
Peak nodal von Mises stress (MPa)	458.35	369.27	-19.4%
Maximum equivalent plastic strain	—	0.000702	—
Plastic-zone extent near hole edge	—	Sub-millimeter band at hole edge	—
Maximum total deformation (mm)	0.59362	0.58916	-0.8%
Stress-margin indicator	0.60216	0.747	+24.1%

The elastoplastic results reveal that: (i) the peak stress is reduced to approximately 369.27 MPa due to local stress redistribution; (ii) this localized von Mises value should not be directly compared with the uniaxial ultimate tensile

strength as a fracture criterion, because it represents a multiaxial equivalent stress at a constrained notch under localized plastic flow; (iii) plastic straining is confined to a sub-millimeter band at the immediate hole edge, with the maximum equivalent plastic strain reaching 0.000702; and (iv) the maximum total deformation changes only slightly from 0.59362 mm in the linear-elastic analysis to 0.58916 mm in the elastoplastic analysis. This confirms that the overall structural stiffness is governed by the elastic bulk of the shell rather than by the localized plastic zone.

These findings are consistent with the Neuber rule (Neuber, 1961), which provides a theoretical estimate of the elastoplastic stress-strain state from the linear-elastic solution. In this framework, the local stress-strain product at the notch is related to the corresponding linear-elastic concentration state; intersection with the material stress-strain curve moderates the apparent peak stress and therefore qualitatively corroborates the FE result.

The following conclusions are drawn:

1. The linear-elastic peak stress of 458.35 MPa is a nominal indicator of stress concentration severity, not a prediction of actual post-yield material stress. Once plasticity is accounted for, stress redistribution limits the local equivalent stress to a level governed by the adopted hardening model and the surrounding elastic constraint.

2. The plastic zone is highly localized around the mounting holes and does not compromise the global load-bearing capacity under the single-pulse condition studied.

3. For comparative ranking of the three shell configurations, the linear-elastic metric remains useful because the relative ordering of stress concentration among the three schemes is preserved under the supplementary plasticity check.

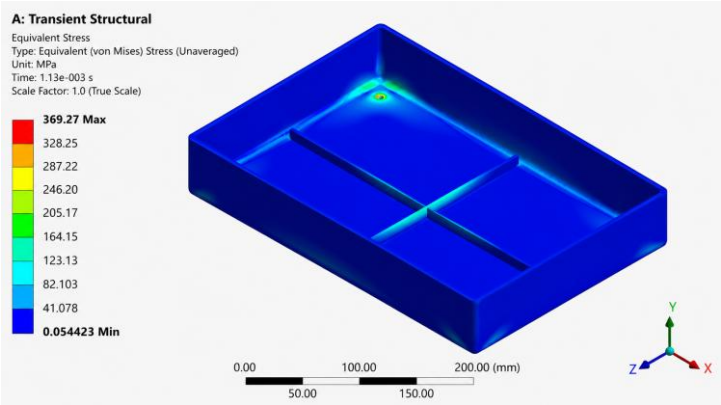

Figure 10. Overall elastoplastic von Mises stress distribution for the 4/4 mm + stiffener shell at the peak response time (t ~ 1.13 ms).

The peak unaveraged nodal stress of 369.27 MPa is located at the cross-rib intersection near the mounting hole, reduced by 19.4% from the linear-elastic prediction (458.35 MPa). The global stress field retains the same qualitative distribution as the linear-elastic case, with local stress relief at the hole edge due to plastic redistribution.

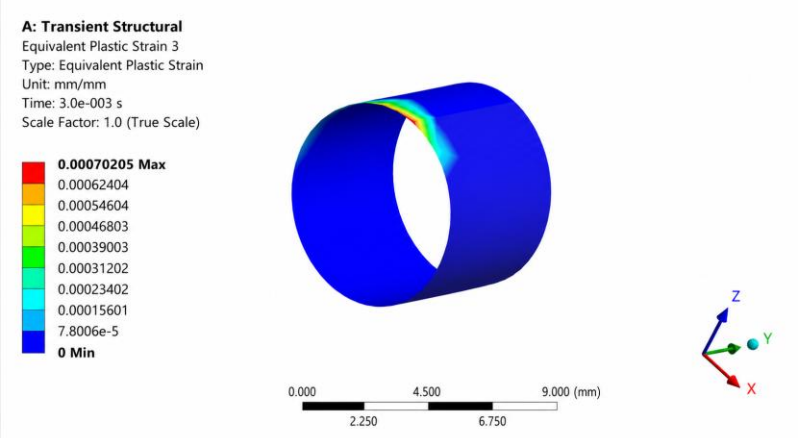

Figure 11. Equivalent plastic strain (EPPLEQV) distribution at the mounting hole edge (peak = 0.0007).

The plastic strain is exclusively localized at the hole periphery, confirming yielding is confined to a sub-millimeter band within the first element layer. No plastic penetration into the shell wall cross-section is observed; the remainder of the structure remains purely elastic.

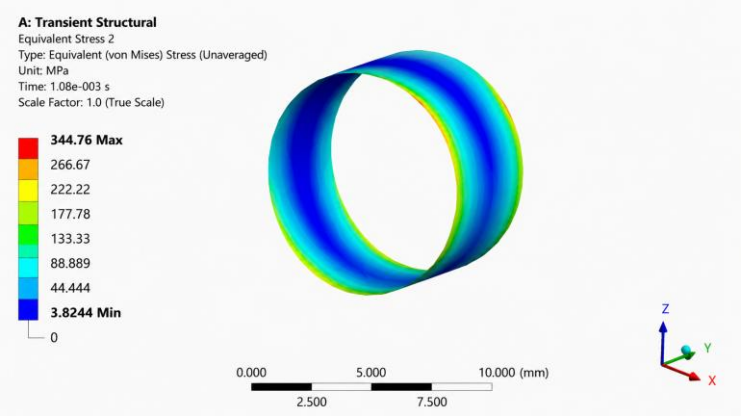

Figure 12. Detail view of elastoplastic von Mises stress at the hole edge.

At the hole edge, the peak equivalent stress reaches 369.27 MPa and is confined to the immediate hole-edge region. This localized value should be interpreted together with the very small maximum equivalent plastic strain of 0.000702 rather than as a direct uniaxial tensile-failure criterion. The rapid stress decay away from the hole edge further indicates that plastic redistribution is geometrically localized and does not penetrate through the shell wall.

Limitations. The present elastoplastic check is limited to a single-pulse analysis of the most critical stiffened configuration. Repeated-impact fatigue, strain-rate effects, and ductile damage accumulation are outside the scope of this comparative study and should be examined in future experimental or nonlinear validation work.

3.6 Validation Considerations

Experimental validation against instrumented impact tests was not available within the scope of the present numerical study. Nevertheless, the following considerations support the credibility of the comparative trends drawn from the FE results.

First, the numerical methodology adopted here is consistent with FE frameworks reported in the literature for related impact and perforated-plate problems. Her and Lan (2014) compared ANSYS/LS-DYNA simulations of an aluminum plate under drop testing with measured acceleration and strain responses. Liu and Liaw (2009) combined drop-weight impact tests with LS-DYNA simulations for cast acrylic/aluminum plates while examining geometric parameters, including holes. Konieczny et al. (2020) also compared ANSYS-based von Mises stress distributions for circular perforated plates with experimental stress measurements. These studies do not directly validate the present enclosure model, but they support the suitability of transient FE analysis for comparative assessment when mesh and boundary-condition checks are included.

Second, the mesh sensitivity analysis (Section 2.4) and the constraint condition comparison (Section 2.5) serve as internal consistency checks. The relative ordering of the three shell configurations was preserved across all mesh densities and idealized boundary conditions. This invariance indicates that the comparative conclusions are robust with respect to the modeling assumptions that inevitably accompany a purely numerical approach.

It is acknowledged that the absolute peak stress values reported herein have not been directly corroborated by physical experiments and should be interpreted as comparative metrics rather than absolute failure predictions. Dedicated experimental validation including instrumented impact tests with strain gauge arrays placed in the vicinity of mounting holes is planned as a separate investigation and will be reported in due course

3.7 Influence of Bolted Connection Idealization

The present FE model idealizes the bolted connection by fully constraining the inner surfaces of the mounting holes, an assumption that represents the limiting case of a perfectly rigid fastener with infinite preload and no interfacial slip. In practice, a bolted joint involves three additional physical mechanisms that are not captured by this idealization, each of which is discussed below.

(1) Bolt preload. A properly torqued bolt introduces a compressive clamping stress around the hole periphery. Under some preload-dominated contact states, this pre-compression may partially offset the tensile stress concentration at the

hole edge. Accordingly, the fully constrained idealization can be regarded as a conservative stress-assessment case for the present comparative model, although a quantitative preload effect would require an explicit contact-preload bolted-joint simulation (Bickford, 2007).

(2) Frictional slip at the contact interface. Under sufficient lateral impact load, microscopic or macroscopic slip may occur at the shell-to-baseplate interface before the bolt comes into bearing contact. Such slip can dissipate energy, reduce the instantaneous force transmitted through the constraint, and increase global displacement relative to the perfectly bonded assumption. The global deformation values reported in Sections 3.2-3.4 should therefore be regarded as lower-bound estimates under the adopted idealized support.

(3) Assembly clearance. Manufacturing tolerances inevitably introduce a small radial gap between the bolt shank and the hole wall. Under impact, the shell undergoes an initial free-flight phase until this gap is closed, after which the bolt engages in bearing. This sequence can generate an impulsive reaction force that amplifies the local contact stress beyond the quasi-steady prediction of a permanently engaged constraint. Quantifying this effect requires explicit contact modeling with initial clearance, which falls outside the scope of the present comparative study.

In summary, the idealized constraints adopted in this work intentionally represent a conservative scenario for hole-edge stress evaluation while potentially underestimating global deformation. This conservatism is deemed acceptable for a comparative ranking study, where the primary objective is to identify the most critical shell configuration rather than to predict absolute performance.

3.8 Discussion of Impact Parameter Sensitivity

The present study considered a single transient acceleration pulse representative of a 300 *g* impact environment. In practice, impact conditions vary in pulse width, peak amplitude, and repetition. Although a full parametric sweep falls beyond the scope of this comparative study, the implications of these variations are discussed qualitatively.

(1) Pulse width. The dynamic response of a thin-walled shell depends on the relationship between the pulse duration and the characteristic structural period. If the impact pulse is much shorter than the structural period, the response approaches an impulse-dominated regime in which peak deformation is governed strongly by the total impulse. Conversely, a pulse width much longer than the structural period tends to drive a quasi-static response. A parametric sweep of pulse widths would be required to identify the worst-case condition for each shell configuration.

(2) Impact energy. Within the elastic regime, stress and deformation are expected to scale approximately with the peak acceleration under the same pulse shape. Once localized yielding initiates at the hole edge, however, additional impact energy may be partly absorbed through plastic-zone expansion rather than through proportional stress growth. Therefore, the comparative ranking obtained from the linear-elastic analysis should be rechecked by elastoplastic analysis when higher impact amplitudes are considered.

(3) Multiple impacts. Repeated impact loading introduces low-cycle fatigue as a potential failure mode distinct from the single-pulse overload considered here. The elastoplastic analysis shows that plastic strain is confined to the hole-edge region. Under cyclic loading, this localized plastic zone may accumulate damage with each successive pulse, leading to crack initiation at a stress level well below the monotonic ultimate strength. The 4/4 mm + stiffener configuration, which exhibited the highest elastic stress concentration, is expected to be the most vulnerable to multi-pulse fatigue. Systematic cyclic plasticity analysis is recommended as future work for applications involving repeated impact exposure.

4 MASS-RELATED IMPACT RESISTANCE EFFICIENCY

To avoid evaluating structural schemes only by absolute response values, the 4/4 mm baseline scheme is used as the reference. A mass-related impact-resistance efficiency index is introduced to assess the benefit under lightweight constraints from three perspectives: deformation control, stress control, and local linear-elastic stress margin. Similar lightweight assessment ideas are useful for structural impact design because absolute deformation reduction may be achieved at the cost of excessive mass or increased local damage risk (Yao et al., 2016; Cheng et al., 2023). Therefore, the mass ratio is defined as follows:

$$\lambda_m = m_i / m_o \tag{4}$$

Further define the unit mass displacement control efficiency, stress control efficiency, and stress-margin efficiency:

$$\eta_\delta = (\delta_o / \delta_i) / (m_i / m_o) \quad (5)$$

$$\eta_\sigma = (\sigma_o / \sigma_i) / (m_i / m_o) \quad (6)$$

$$\eta_n = (n_i / n_o) / (m_i / m_o) \quad (7)$$

where δ_o and δ_i represent the maximum total deformations of the baseline and comparison schemes, respectively; σ_o and σ_i denote the nodal peak equivalent stresses; and n_o and n_i indicate the minimum linear-elastic stress-margin indicators. When $\eta > 1$, the scheme provides a positive performance benefit per unit mass. When $\eta < 1$, the improvement of a given metric is insufficient to compensate for the mass cost or the associated local risk. These indicators are comparative engineering metrics rather than universal material constants, and their interpretation is tied to the same loading and modelling assumptions (Yu et al., 2021; Yao et al., 2016; Cheng et al., 2023).

Table 8. Mass-related impact resistance efficiency based on the 4/4 mm baseline scheme.

Scheme	Mass ratio m_i/m_o	η_δ	η_σ	η_n
4/4 mm + stiffeners	1.0138	1.175	0.744	0.744
5/5 mm	1.2372	1.402	0.978	0.978

The displacement efficiency of the 4/4 mm locally stiffened scheme is 1.175, indicating enhanced deflection control with a slight mass increase. However, both the stress efficiency and stress-margin efficiency are 0.744, showing that this scheme achieves deformation reduction at the cost of higher local stress and a lower elastic margin. The 5/5 mm uniformly thickened scheme has the highest displacement efficiency, with $\eta\delta = 1.402$. Its stress efficiency and stress-margin efficiency are both approximately 0.978, which are clearly higher than those of the locally stiffened scheme but slightly below unity due to the additional mass penalty. Thus, under the specified loading conditions, uniform thickening provides the most balanced absolute improvement, however, these stress-related benefits must be weighed against the accompanying mass gain.

5 DISCUSSION, LIMITATIONS AND DESIGN RECOMMENDATIONS

The findings indicate that the impact resistance of perforated thin-walled shells is governed not only by whether a stiffener is introduced, but also by the uniformity of load transfer, the smoothness of local structural transitions, and the stress relief capacity around mounting holes. The unfavorable local performance of the 4/4 mm locally stiffened scheme does not imply that stiffeners are inherently unsuitable. Instead, it shows that the current stiffener layout improves bending stiffness in the plate region while failing to relieve stress near the mounting holes. This agrees with stiffened-plate and perforated-plate studies showing that reinforcement layout, relative stiffness, openings, and load-transfer paths jointly affect dynamic response and local risk regions (Zhao et al., 2020; Goel et al., 2011; Jiang et al., 2023; Li et al., 2017; Xu et al., 2005; Abu-Farsakh et al., 2015).

A second important issue is the boundary condition. The fixed-hole approximation is useful for maintaining a controlled comparison, however, it is a simplified representation of bolted support. In real assemblies, bolt preload, local contact, joint clearance, and fixture flexibility may redistribute the stress field near the holes. The boundary-condition sensitivity check in Section 2.5 reduces this uncertainty by replacing the fixed-hole support with a relaxed hole-support condition while retaining the same geometry, mesh, load history, and solver settings. The relaxed support changes the absolute hole-edge peak stress, but it does not reverse the main trend: the locally stiffened scheme still reduces deformation while showing higher local stress risk and a lower elastic stress margin than the corresponding 4/4 mm baseline. Therefore, the fixed-hole model should be understood as a conservative comparative framework rather than a complete bolted-joint failure model.

Representative relaxed-support contours are shown in Figure 13 to document the sensitivity check visually. They support the numerical trend in Table 5: releasing the tangential constraint modifies the absolute peak stress, however, the locally stiffened shell still shows more pronounced stress concentration and a lower stress margin than the corresponding 4/4 mm baseline.

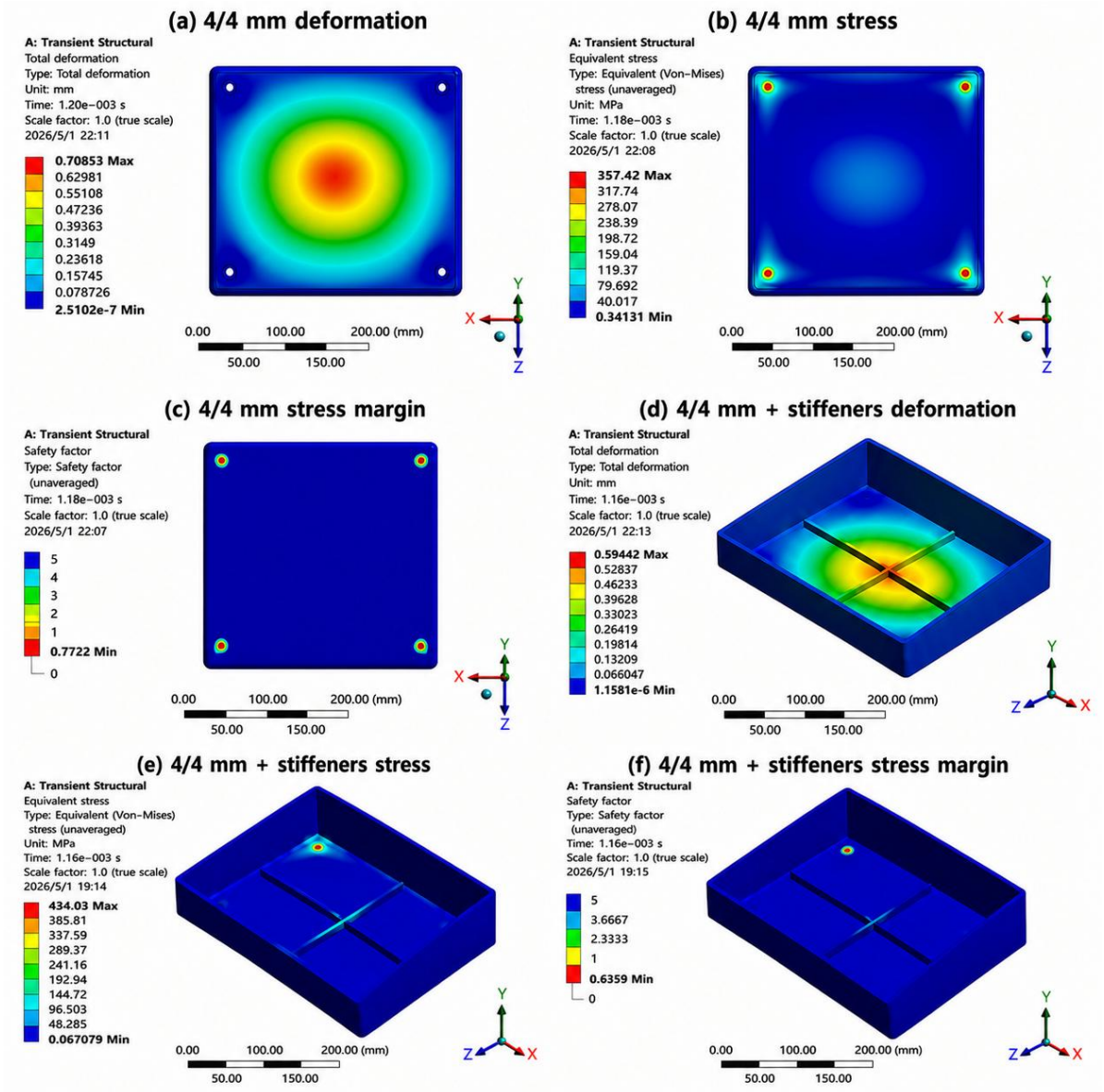

Figure 13. Representative contour results from the relaxed hole-support sensitivity check: (a-c) deformation, equivalent stress, and stress-margin contours of the 4/4 mm baseline shell; (d-f) corresponding contours of the 4/4 mm shell with local stiffeners. The contours visually confirm that the support idealization changes the absolute stress level but does not reverse the comparative trend.

The linear-elastic material model is a deliberate limitation of this preliminary comparative study. When the calculated unaveraged nodal peak stress exceeds the yield strength or tensile strength of 6061-T6 aluminum, the value should be interpreted as a conservative stress-concentration indicator rather than a direct failure prediction. The supplementary elastoplastic results provide the necessary qualification: the contours in Figures 10-12 visually confirm that yielding is confined to the immediate hole periphery, while the global stress field remains essentially consistent with the linear-elastic distribution. Thus, the linear-elastic ranking remains useful for comparative design screening, but final acceptance of a locally stiffened scheme still requires elastoplastic verification and hole-edge reinforcement assessment.

For high-reliability protective enclosures, the 5/5 mm uniformly thickened scheme should be prioritized as the more balanced candidate under the specified impact conditions. However, because its minimum linear-elastic stress-margin indicator remains slightly below unity when unaveraged nodal peak stress is used, additional hole-edge reinforcement, smoother local transitions, or elastoplastic assessment is still recommended for strict strength design. If local stiffening must be adopted due to lightweight constraints, the stiffener layout should be redesigned together with hole-edge reinforcement, rounded stiffener-end transitions, sufficient distance between stiffener terminations and holes, and subsequent elastoplastic assessment. These recommendations are consistent with lightweight enclosure design and

stress-concentration considerations when holes and local reinforcement coexist in protective shell structures (Li et al., 2017; Abu-Farsakh et al., 2015; Cheng et al., 2023).

6 CONCLUSIONS

The present study investigated stiffness redistribution and hole-edge stress concentration in three thin-walled 6061-T6 aluminum shell configurations under transient impact loading. The main contributions and findings are as follows:

(1) Stiffness redistribution mechanism. Local stiffening introduces a previously underexplored trade-off in lightweight enclosure design: while adding stiffeners or thickening the shell wall reduces global deformation, it simultaneously redistributes internal load paths, concentrating stress toward geometric discontinuities, particularly the mounting holes. This redistribution effect is the central finding of this work.

(2) Quantitative comparison. Among the three configurations, the 5/5 mm uniformly thickened shell achieved the greatest deformation reduction (42.36%) along with a 17.34% reduction in nodal peak stress and a stress-margin indicator of 0.96538. The 4/4 mm + stiffener configuration reduced maximum total deformation by 16.06% compared with the baseline, yet the peak unaveraged nodal von Mises stress increased by 32.52% to 458.35 MPa, exceeding both the yield strength (276 MPa) and ultimate tensile strength (310 MPa) of the material.

(3) Plasticity assessment. A supplementary elastoplastic analysis using a BISO model demonstrated that the linear-elastic peak of 458.35 MPa is a nominal comparative metric rather than a prediction of actual elastic stress. After plastic redistribution, the peak nodal von Mises stress decreases to 369.27 MPa, and plastic straining is confined to a sub-millimeter band around the hole edge, with the maximum equivalent plastic strain reaching 0.000702. The localized elastoplastic von Mises stress should not be directly compared with the uniaxial ultimate tensile strength as a fracture criterion. The elastoplastic contours indicate that the global stress field remains essentially unchanged, so the linear-elastic ranking is conservative but still useful for comparative design assessment.

(4) Boundary condition sensitivity. The constraint condition at the mounting holes significantly affects absolute stress magnitude, although the relative ranking among the three shell schemes remains consistent under both fixed and relaxed hole-support idealizations, supporting the robustness of the comparative conclusions.

(5) Mass efficiency and design implication. Mass-related efficiency analysis confirms that uniform thickening provides a more balanced improvement across deformation, stress, and stress-margin indicators. For impact-resistant thin-walled shells, global deformation cannot serve as the sole design criterion. The stiffness redistribution phenomenon requires that hole-edge stress concentration be explicitly evaluated. A configuration that appears optimal by displacement metrics may be the most vulnerable by local strength criteria.

(6) Discussion of modeling idealizations. Bolt preload, frictional slip, and assembly clearance are discussed qualitatively. The fully constrained hole idealization adopted herein provides a conservative stress-assessment case while potentially underestimating global deformation, which is acceptable for a comparative ranking study. The present conclusions are most directly applicable to the specified 300 g, 2 ms single-pulse condition; pulse-width sweeps, higher-energy impacts, contact-preload bolted-joint modeling, experimental validation, and repeated-impact fatigue require further nonlinear or experimental verification.

Acknowledgements

This research was supported by the Civil Aerospace Technology Pre-Research Program (Grant No. D020110). The authors would like to gratefully acknowledge this support.

Author's Contributions: Conceptualization, Xichen Deng; Methodology, Xichen Deng; Software, Xichen Deng; Formal analysis, Xichen Deng; Investigation, Xichen Deng; Visualization, Xichen Deng; Writing - original draft, Xichen Deng; Supervision, Yanqing Guo; Validation, Yanqing Guo; Project administration, Yanqing Guo; Writing - review and editing, Lu Liu.

Data Availability: Research data are available from the corresponding author upon reasonable request.

Editor: Marcilio Alves

References

Abu-Farsakh, G.A., Almasri, A.H., Qa'dan, D.H., (2015). Stress concentration around a central hole as affected by material nonlinearity in fibrous composite laminated plates subject to in-plane loading. Science and Engineering of Composite Materials 22(1):31-36. doi:10.1515/secm-2013-0125.

ASM Handbook, Volume 2: Properties and Selection: Nonferrous Alloys and Special-Purpose Materials, (1990). 10th ed. ASM International, Materials Park, OH.

Bickford, J.H., (2007). Introduction to the Design and Behavior of Bolted Joints: Non-Gasketed Joints, 4th ed. CRC Press, Boca Raton.

Cao, Y., Zhong, R., Shao, D., Wang, Q., Guan, X., (2019). Dynamic analysis of rectangular plate stiffened by any number of beams with different lengths and orientations. Shock and Vibration 2019:2364515. doi:10.1155/2019/2364515.

Cheng, Z., Li, H., Li, Z., Chen, Y., Chang, J., Li, X., (2023). Structural lightweight design and experimental validation for aerospace sealed cabin. Frontiers in Mechanical Engineering 9:1265734. doi:10.3389/fmech.2023.1265734.

Geretto, C., Yuen, S.C.K., Nurick, G.N., (2015). An experimental study of the effects of degrees of confinement on the response of square mild steel plates subjected to blast loading. International Journal of Impact Engineering 79:32-44. doi:10.1016/j.ijimpeng.2014.08.002.

Goel, M.D., Matsagar, V.A., Gupta, A.K., (2011). Dynamic response of stiffened plates under air blast. International Journal of Protective Structures 2(1):139-155. doi:10.1260/2041-4196.2.1.139.

Her, S.C., Lan, S.C., (2014). Dynamic analysis of an aluminum plate subjected to drop test. Journal of Applied Mechanical Engineering 3:e130. doi:10.4172/2168-9873.1000e130.

Jiang, W., Han, G., Zhang, Y., (2023). Impacts of natural frequency and relative stiffness of stiffened plate on nonlinear dynamic response. Chinese Journal of Ship Research 18(1):223-230. doi:10.19693/j.issn.1673-3185.02515.

Konieczny, M.M., Achtelik, H., Gasiak, G., (2020). Finite element analysis (FEA) and experimental stress analysis in circular perforated plates loaded with concentrated force. Frattura ed Integrità Strutturale 14(51):164-173. doi:10.3221/IGF-ESIS.51.13.

Langdon, G.S., Yuen, S.C.K., Nurick, G.N., (2005). Experimental and numerical studies on the response of quadrangular stiffened plates. Part II: Localised blast loading. International Journal of Impact Engineering 31(1):85-111. doi:10.1016/j.ijimpeng.2003.09.050.

Li, Y., Ren, X., Zhao, T., Xiao, D., Liu, K., Fang, D., (2021). Dynamic response of stiffened plate under internal blast: Experimental and numerical investigation. Marine Structures 77:102957. doi:10.1016/j.marstruc.2021.102957.

Li, Y., Wu, W., Zhu, H., Wu, Z., Du, Z., (2017). The influence of different pre-formed holes on the dynamic response of square plates under air-blast loading. Engineering Failure Analysis 78:122-133. doi:10.1016/j.engfailanal.2017.03.002.

Liu, Y., Liaw, B., (2009). Drop-weight impact tests and finite element modeling of cast acrylic/aluminum plates. Polymer Testing 28(8):808-823. doi:10.1016/j.polymertesting.2009.07.003.

Nagesh, Gupta, N.K., (2021). Response of thin walled metallic structures to underwater explosion: A review. International Journal of Impact Engineering 156:103950. doi:10.1016/j.ijimpeng.2021.103950.

Neuber, H., (1961). Theory of stress concentration for shear-strained prismatical bodies with arbitrary nonlinear stress-strain law. Journal of Applied Mechanics 28(4):544-550. doi:10.1115/1.3641780.

Nurick, G.N., Martin, J.B., (1989a). Deformation of thin plates subjected to impulsive loading - A review. Part I: Theoretical considerations. International Journal of Impact Engineering 8(2):159-170. doi:10.1016/0734-743X(89)90014-6.

Nurick, G.N., Martin, J.B., (1989b). Deformation of thin plates subjected to impulsive loading - A review. Part II: Experimental studies. International Journal of Impact Engineering 8(2):171-186. doi:10.1016/0734-743X(89)90015-8.

Xu, X.D., Lee, H.P., Lu, C., (2005). Power flow paths in stiffened plates. Journal of Sound and Vibration 282(3-5):1264-1272. doi:10.1016/j.jsv.2004.05.011.

Yao, S., Chen, Y., Sun, C., Zhao, N., Wang, Z., Zhang, D., (2024). Dynamic response mechanism of thin-walled plate under confined and unconfined blast loads. Journal of Marine Science and Engineering 12(2):224. doi:10.3390/jmse12020224.

Yao, S., Zhang, D., Lu, F., (2016). Dimensionless number for dynamic response analysis of box-shaped structures under internal blast loading. International Journal of Impact Engineering 98:13-18. doi:10.1016/j.ijimpeng.2016.07.005.

Yu, T., Zhu, L., Xu, J., (2021). Progress in structural impact dynamics during 2010-2020. Explosion and Shock Waves 41(12):121401. doi:10.11883/bzycj-2021-0113.

Yuen, S.C.K., Nurick, G.N., (2005). Experimental and numerical studies on the response of quadrangular stiffened plates. Part I: Subjected to uniform blast load. International Journal of Impact Engineering 31(1):55-83. doi:10.1016/j.ijimpeng.2003.09.048.

Zhang, D., Yao, S., Lu, F., Song, J., Ding, Y., (2019). Dynamic response and damage analysis of steel box wall under internal blast loading. Advances in Mechanical Engineering 11(1):1-11. doi:10.1177/1687814018822601.

Zhao, N., Yao, S., Zhang, D., et al., (2020). Experimental and numerical studies on the dynamic response of stiffened plates under confined blast loads. Thin-Walled Structures 154:106839. doi:10.1016/j.tws.2020.106839.

Zheng, C., Kong, X.S., Wu, W.G., Liu, F., (2016). The elastic-plastic dynamic response of stiffened plates under confined blast load. International Journal of Impact Engineering 95:141-153. doi:10.1016/j.ijimpeng.2016.05.008.